Darcy-scale modeling of microbially induced carbonate mineral precipitation in sand columns

A. Ebigbo,[1] A. Phillips,[2] R. Gerlach,[2,3] R. Helmig,[1] A. B. Cunningham,[2,3] H. Class,[1] and L. H. Spangler[3]

Received 5 December 2011; revised 16 May 2012; accepted 7 June 2012; published 28 July 2012.

[1] This investigation focuses on the use of microbially induced calcium carbonate precipitation (MICP) to set up subsurface hydraulic barriers to potentially increase storage security near wellbores of CO_2 storage sites. A numerical model is developed, capable of accounting for carbonate precipitation due to ureolytic bacterial activity as well as the flow of two fluid phases in the subsurface. The model is compared to experiments involving saturated flow through sand-packed columns to understand and optimize the processes involved as well as to validate the numerical model. It is then used to predict the effect of dense-phase CO_2 and CO_2-saturated water on carbonate precipitates in a porous medium.

Citation: Ebigbo, A., A. Phillips, R. Gerlach, R. Helmig, A. B. Cunningham, H. Class, and L. H. Spangler (2012), Darcy-scale modeling of microbially induced carbonate mineral precipitation in sand columns, *Water Resour. Res.*, *48*, W07519, doi:10.1029/2011WR011714.

1. Introduction

[2] Mineral precipitation influenced by microbial activity in the subsurface (particularly through the urea-hydrolysis pathway), commonly referred to a microbially induced calcium carbonate precipitation (MICP), can be exploited for a variety of engineered applications including the immobilization of groundwater contaminants [*Ferris et al.*, 2003; *Fujita et al.*, 2010, 2004, 2008], ground reinforcement or altering properties of porous materials [*DeJong*, 2006; *Harkes et al.*, 2010; *Ivanov and Chu*, 2008; *van Paassen et al.*, 2010; *Whiffin et al.*, 2007], and the creation of hydraulic barriers for purposes such as enhanced oil recovery or increasing storage security of CO_2 [*Cunningham et al.*, 2009, 2011; *Ebigbo et al.*, 2010; *Ferris et al.*, 1996]. Many organisms are capable of hydrolyzing urea, which can alter the saturation state of the formation water, and in the presence of calcium, may favor the precipitation of calcium carbonate [*Ferris et al.*, 2003; *Mobley and Hausinger*, 1989; *Stumm and Morgan*, 1996].

[3] In previous studies, greater calcium carbonate precipitation was observed near injection sites which could potentially lead to restricted transport of nutrients and have adverse effects on well injectivity [*Fujita et al.*, 2008; *Whiffin et al.*, 2007]. Before a biomineralization technology can be considered field relevant, mineral deposition must be demonstrated to be controllable at a relevant scale while maintaining economic feasibility [*Harkes et al.*, 2010]. Controlling mineralization has been investigated by balancing the reaction with transport, for example, altering injection strategies or injection rates, manipulating the reactant concentrations, increasing the number of applications of treatments, or controlling the distribution of active microbes [*De Muynck et al.*, 2010a; *Harkes et al.*, 2010; *Whiffin et al.*, 2007]. Additionally, it has been reported that the types and sizes of crystals formed are affected by the number and form (planktonic or attached) of cells, and that the environmental conditions in surrounding fluids can affect precipitation [*Achal et al.*, 2009b; *Cuthbert et al.*, 2012; *Dupraz et al.*, 2009a, 2009b; *Mitchell and Ferris*, 2006; *Mortensen et al.*, 2011; *Tobler et al.*, 2011]. Multiscale and extensive cross-disciplinary research on the feasibility of such a technology is key for its successful implementation [*DeJong et al.*, 2010, 2012].

[4] The challenges to creating effective and extensive hydraulic barriers for increasing CO_2 storage security are to make efficient use of resources and to promote mineralization in the regions of interest without plugging other regions. Analyzing all combinations of these precipitation-influencing factors in the laboratory would be laborious and time consuming. Several other researchers have utilized models to assist in the understanding or optimization of MICP treatment technologies [*Barkouki et al.*, 2011; *Fauriel and Laloui*, 2011; *van Wijngaarden et al.*, 2011; *Zhang and Klapper*, 2010]. The model described in this paper was also developed to quickly analyze parameters and optimize experimental efforts with the aim of improving the understanding of the relevant processes involved. The bench-scale column results and Darcy-scale modeling efforts reported here address the challenge of demonstrating control of mineral deposition (i.e., $CaCO_3$) uniformly along the flow path in a porous medium.

[5] Four separate column experiments were performed in order to: develop an injection strategy to produce

[1]Department of Hydromechanics and Modeling of Hydrosystems, University of Stuttgart, Stuttgart, Germany.
[2]Center for Biofilm Engineering, Montana State University, Bozeman, Montana, USA.
[3]Energy Research Institute, Montana State University, Bozeman, Montana, USA.

Corresponding author: A. Ebigbo, Department of Hydromechanics and Modeling of Hydrosystems, University of Stuttgart, Pfaffenwaldring 61, 70569 Stuttgart, Germany. (anozie.ebigbo@iws.uni-stuttgart.de)

0043-1397/12/2011WR011714

homogenous $CaCO_3$ distribution along the length of the column, calibrate the model, and validate the model by comparing it to the physical data.

[6] Finally, while not supported by experimental data, the model also examines some of the potential interactions of dense-phase CO_2 with $CaCO_3$. The model simulates two-fluid-phase (water and CO_2) experiments, providing a useful tool for the optimization of injection strategies, the design of high-pressure CO_2 experiments, and, ultimately, prospective field-scale application.

2. Model Description

[7] The system of interest consists of two fluid phases (water and CO_2), three immobile phases (rock/porous medium, calcite precipitates, and biofilm), and suspended/dissolved components (see Figure 1). It shall be noted that other calcium carbonate morphotypes are possible products of the ureolysis-induced calcium carbonate precipitation process described in this work. However, calcite is the most frequently described calcium carbonate morphotype observed and was chosen as the representative morphotype in this model. In addition, biofilm as described here refers to attached microorganisms capable of producing extracellular polymeric substances (EPS) [*Cuthbert et al.*, 2012; *Schultz et al.*, 2011].

[8] Here the system is addressed on the so-called Darcy (macro) scale which is obtained if the processes on the pore (micro) scale can be averaged adequately [*Bear*, 1972; *van Duijn and Pop*, 2004; *van Noorden*, 2009a, 2009b, 2010; *Golfier et al.*, 2009]. In this article, the equations and variables of the model are defined on the macroscale. Thus, only volume-averaged information is available within a *representative elementary volume*.

2.1. Definition of System and Main Assumptions

[9] The components the model accounts for include water (w), carbon dioxide (CO_2), suspended biomass (b), attached biomass/biofilm (f), substrate (s), electron acceptor/oxygen (e), calcite (c), urea (u), ammonia/ammonium (a), calcium (Ca^{2+}), chloride (Cl^-), and sodium (Na^+).

[10] Two fluid phases may be present in the pores of the porous medium (water [w] and CO_2 [n]), which are the wetting and the nonwetting phases, respectively. Before the injection of CO_2, only water is present. Thus, the set of primary variables can change depending on the number of phases present [*Class et al.*, 2002].

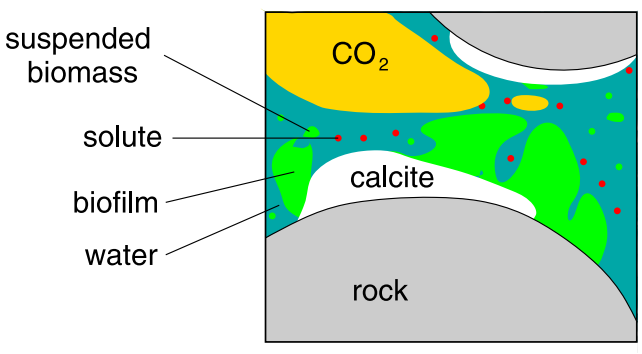

Figure 1. Schematic porescale representation of system of interest.

[11] The water phase consists of the components water, dissolved CO_2, suspended biomass, substrate, oxygen, urea, ammonia/ammonium, calcium, chloride, and sodium. The CO_2 phase consists of CO_2, water, and oxygen. All other components are assumed not to dissolve/partition into this phase. Calcite and biofilm are immobile.

[12] Even though brines consist of several salts, it is assumed here that their combined effect on density, viscosity, and CO_2 solubility can be represented by an equivalent sodium chloride concentration [*Michaelides*, 1981].

[13] There is no differentiation between molecularly dissolved CO_2 and carbonic acid. The sum of both is referred to as H_2CO_3 [*Chou et al.*, 1989; *Flukiger and Bernard*, 2009].

[14] In the explanations and diagrams that follow, it is assumed that the host rock (or other porous medium) does not contain significant amounts of carbonate minerals. However, if this is not the case, the amount of calcite initially present in the model can be set to a nonzero value.

2.2. Chemical Reactions

[15] In the presence of the enzyme urease, urea is hydrolyzed to give ammonia and carbonic acid. The bacterial strain *Sporosarcina pasteurii* is capable of producing large amounts of urease [*Ciurli et al.*, 1996]. The subsequent protonation of ammonia to ammonium causes an increase in pH, shifting the equilibrium of the calcite precipitation/dissolution reaction toward precipitation by increasing the availability of the carbonate ion (CO_3^{2-}).

$$CO(NH_2)_2 + 2H_2O \xrightarrow{\text{urease}} 2NH_3 + H_2CO_3 \quad \text{ureolysis}$$
$$2NH_3 + 2H_2O \leftrightarrow 2NH_4^+ + 2OH^- \quad \text{protonation of ammonia}$$
$$H_2CO_3 + OH^- \leftrightarrow HCO_3^- + H_2O \quad \text{dissociation of carbonic acid}$$
$$HCO_3^- + OH^- \leftrightarrow CO_3^{2-} + H_2O \quad \text{dissociation of bicarbonate ion}$$
$$Ca^{2+} + CO_3^{2-} \leftrightarrow CaCO_3 \downarrow \quad \text{calcite precipitation/dissolution.}$$

[16] The dissociation reactions are fast compared to ureolysis, precipitation, and dissolution. Hence, these are assumed to occur instantaneously and are accounted for with equilibrium coefficients. Slower reactions are described by using rate expressions.

2.2.1. Rate of Ureolysis

[17] As described by *Fidaleo and Lavecchia* [2003], the rate of urea hydrolysis is given by,

$$r_{\text{urea}} = \nu_{\max} Z_{\text{ub}} \frac{m_{\text{u}}}{(K_{\text{u}} + m_{\text{u}})\left(1 + \frac{m_{NH_4^+}}{K_{NH_4^+}}\right)}, \tag{1}$$

where m_{u} is the molality of urea, K_{u} is the Monod half-saturation constant, and $K_{NH_4^+}$ is an inhibition parameter due to high NH_4^+ concentrations. The maximum rate of ureolysis $\nu_{\max}$ is calculated as follows:

$$\nu_{\max} = \frac{k}{1 + \frac{m_{H^+}}{K_{\text{EU},1}} + \frac{K_{\text{EU},2}}{m_{H^+}}}. \tag{2}$$

Dissociation constants for the enzyme-urea complex are denoted by $K_{\text{EU},i}$, and k is a rate constant. Note that these

rate expressions from *Fidaleo and Lavecchia* [2003] were determined for jack beans urease. It is assumed here that the same expressions can be used for microbially produced urease. The concentration of intra- and extracellular urease in the porous medium Z_{ub} is difficult to determine [*Klose and Tabatabai*, 1999]. Urease is released when bacterial cells rupture and may sorb to polymers of the biofilm and to the porous medium [*Lloyd and Sheaffe*, 1973; *Brotherton et al.*, 1976; *Ciurli et al.*, 1996]. For the purposes of this model, it is assumed that most of the urease is associated with the biofilm (either intracellularly or sorbed to biofilm polymers). Hence, the amount of urease is assumed to be related nonlinearly to the amount of attached biomass (i.e., biofilm),

$$Z_{ub} = k_{ub}(\varrho_f \phi_f)^{n_{ub}} . \tag{3}$$

Suspended biomass is not included since its contribution is considered small compared to that of the biofilm [*Li et al.*, 2000; *Resch et al.*, 2005]. Here ϱ_f is the biofilm density (dry mass per unit volume), ϕ_f is the volume fraction of the porous medium occupied by the biofilm, k_{ub} is a proportionality coefficient, and n_{ub} accounts for the nonlinear dependence of Z_{ub} on $\rho_f \phi_f$.

2.2.2. Rate of Calcite Precipitation/Dissolution

[18] The net rate of precipitation or dissolution of calcite is governed by the calcite saturation state Ω which provides a measure of the distance of the system from equilibrium, i.e., $\Omega = 1$,

$$\Omega = \frac{\gamma_{Ca^{2+}} m_{Ca^{2+}} \gamma_{CO_3^{2-}} m_{CO_3^{2-}}}{K_{sp}} . \tag{4}$$

The activity coefficients $\gamma_{Ca^{2+}}$ and $\gamma_{CO_3^{2-}}$ are calculated using Pitzer equations as described by *Wolf et al.* [1989], *Millero et al.* [1984], and *Clegg and Whitfield* [1995]. To this end, the influence of the interactions of all the ions considered are included in the calculations. However, the concentrations of some of the ions are determined using apparent dissociation coefficients as described in section 2.2.3. Figure 2 shows how the activities of calcium and carbonate ions vary with chloride concentration in NaCl and $NaCl_2$ solutions. K_{sp} is the solubility product of calcite.

[19] The rate at which equilibration occurs is assumed to depend on the distance from equilibrium. When $\Omega > 1$, net precipitation occurs, and net dissolution occurs when $\Omega < 1$. There are several empirical approaches for determining these rates. There are also some approaches which obtain the rates from the upscaling of porescale processes [*van Noorden*, 2009a; *van Duijn and Pop*, 2004]. Here common empirical rate functions for precipitation and dissolution are chosen [*Zhong and Mucci*, 1989],

$$r_{prec} = k_{prec} A_{sw} (\Omega - 1)^{n_p} \text{ for } \Omega \geq 1. \tag{5}$$

The empirical parameters k_{prec} and n_p are available in the literature [e.g., *Zhong and Mucci*, 1989]. The specific interfacial surface between solid (i.e., both porous matrix and calcite) and water phases A_{sw} is estimated from the porosity ϕ with an empirical relation [e.g., *Clement et al.*, 1996] as follows:

$$A_{sw} = A_{sw,0} \left(1 - \frac{\phi_c}{\phi_0}\right)^{\frac{2}{3}} . \tag{6}$$

The subscript "0" denotes initial values.

[20] Similarly, the dissolution rate is calculated as given by [*Chou et al.*, 1989; *Compton et al.*, 1989],

$$r_{diss} = (k_{diss,1} m_{H^+} + k_{diss,2}) A_{cw} (1 - \Omega)^{n_d} \text{ for } \Omega < 1. \tag{7}$$

Again, $k_{diss,1}$, $k_{diss,2}$, and n_d are empirical parameters. A_{cw} is the specific interfacial surface between calcite and water phases. Assuming the porous rock matrix originally in place does not dissolve, A_{cw} may differ significantly from A_{sw} as shown in Figures 3 and 4. For small values of ϕ_c (which is the volume fraction of porous medium occupied by calcite), A_{cw} is proportional to ϕ_c, i.e.,

$$A_{cw} = a_c \phi_c , \tag{8}$$

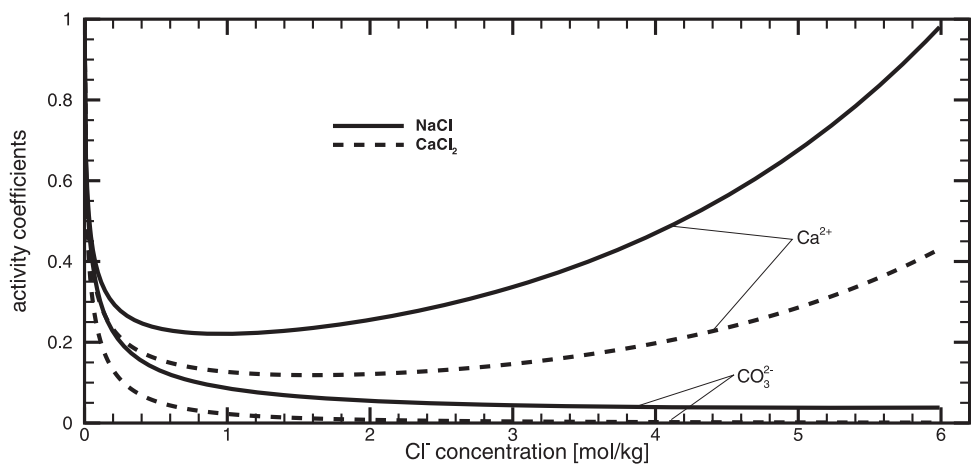

Figure 2. Ca^{2+} and CO_3^{2-} activities as calculated from *Wolf et al.* [1989], *Millero et al.* [1984], and *Clegg and Whitfield* [1995] using Pitzer equations as a function of Cl^- concentration in NaCl and $NaCl_2$ solutions.

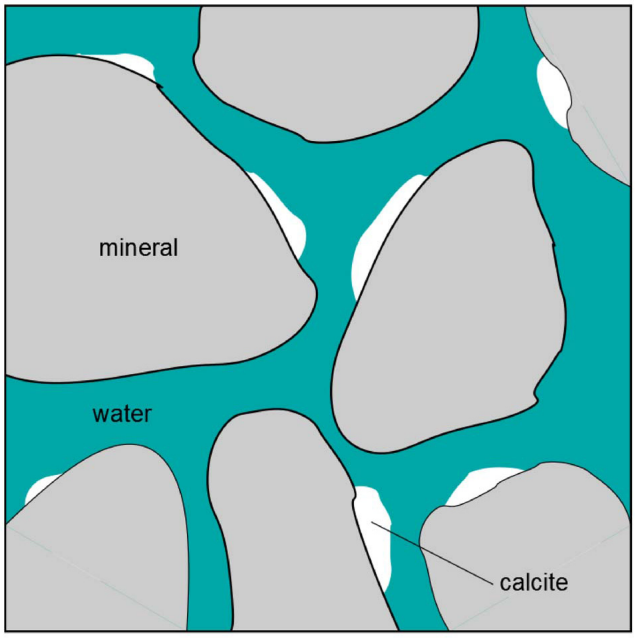

Figure 3. Solid-water interfacial areas: At low values of ϕ_c, the interfacial surface between calcite and water phases, A_{cw}, and that between solid (i.e., both porous matrix and calcite) and water phases, A_{sw}, differ significantly, $A_{cw} < A_{sw}$.

where a_c represents the specific surface area of the calcite grains (surface area per volume of calcite). However, when significant amounts of calcite are present in the porous medium, i.e., for large ϕ_c, this relationship is not valid. Instead,

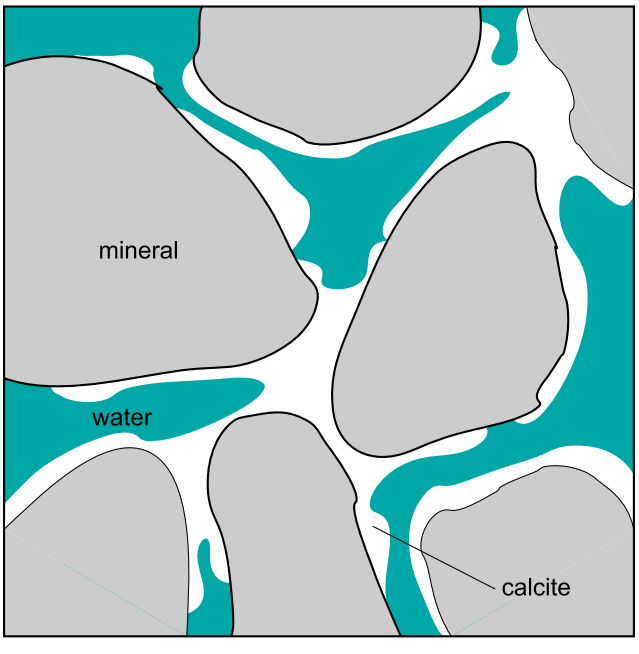

Figure 4. Solid-water interfacial areas: At high values of ϕ_c, the interfacial surface between calcite and water phases, A_{cw}, and that between solid (i.e., both porous matrix and calcite) and water phases, A_{sw}, are equivalent, $A_{cw} \approx A_{sw}$.

A_{cw} and A_{sw} become equivalent. Thus, A_{cw} is chosen in such a way that the limiting of the two options, i.e., the smaller of the two is chosen (see also Figures 3 and 4):

$$A_{cw} = \min\left(A_{sw}, a_c\phi_c\right). \tag{9}$$

2.2.3. Dissociation Coefficients

[21] The dissociation of NH_3 and H_2CO_3 in water are accounted for with *apparent* (i.e., stoichiometric) dissociation coefficients K^*. Calculating activity coefficients as is done for the computation of Ω would unnecessarily increase the complexity and computational cost of the model. As such, correlations from literature are chosen, with which one can determine the apparent dissociation coefficients as functions of ionic strength I,

$$K_a^*(I) = \frac{m_{NH_3} m_{H^+}}{m_{NH_4^+}} \text{ dissociation of ammonia,} \tag{10}$$

$$K_1^*(I) = \frac{m_{HCO_3^-} m_{H^+}}{m_{H_2CO_3}} \text{ dissociation of carbonic acid,} \tag{11}$$

$$K_2^*(I) = \frac{m_{CO_3^{2-}} m_{H^+}}{m_{HCO_3^-}} \text{ dissociation of bicarbonate ion,} \tag{12}$$

$$K_w^*(I) = m_{H^+} m_{OH^-} \text{ dissociation of water.} \tag{13}$$

For H_2CO_3, dissociation coefficients are calculated using correlations given by *Millero et al.* [2007], and those by *Bell et al.* [2008] are used for the dissociation of NH_3. The dissociation coefficient of water is also required and approximated as a function of ionic strength [*Ji*, 1994].

2.3. Mass Balance Equations

[22] Mutual dissolution of the water and CO_2 phases are accounted for with the mass fractions $X_w^{CO_2}$ and X_n^w which represent the amount of CO_2 in the water phase and of water in the CO_2 phase, respectively. Equations which balance the mass of each component in the phases α can be written as in equation (14),

$$\sum_\alpha \left\{ \frac{\partial}{\partial t}(\phi \varrho_\alpha X_\alpha^i S_\alpha) + \nabla \times (\varrho_\alpha X_\alpha^i \mathbf{v}_\alpha) - \nabla \times (\varrho_\alpha \mathbf{D}_\alpha \nabla X_\alpha^i) \right\} = q^i;$$
$$i \in \{w, CO_2\},\ \alpha \in \{w, n\}. \tag{14}$$

Here ϱ is density, S is the fluid-phase saturation within the rock pores, $\mathbf{v}$ is the Darcy flux (fluid-phase velocity), $\mathbf{D}$ is the hydrodynamic dispersion tensor, q represents sources/sinks.

[23] The components which are assumed to exist exclusively as dissolved/suspended components of the water phase can be expressed with concentrations C, and the following mass balance equations hold,

$$\frac{\partial}{\partial t}(\phi S_w C_w^j) + \nabla \times (C_w^j \mathbf{v}_w) - \nabla \times (\mathbf{D}_w \nabla C_w^j) = q^j;$$
$$j \in \{b, s, u, a, Ca^{2+}, Cl^-, Na^+\}. \tag{15}$$

Oxygen can be present in both water and CO_2. Thus, the mass balance equation for oxygen is,

$$\sum_{\alpha}\left\{\frac{\partial}{\partial t}(\phi S_\alpha C_\alpha^{\mathrm{e}}) + \nabla\times(C_\alpha^{\mathrm{e}}\mathbf{v}_\alpha) - \nabla\times(\mathbf{D}_\alpha\nabla C_\alpha^{\mathrm{e}})\right\} = q^e; \quad \alpha\in\{\mathrm{w},\mathrm{n}\}. \tag{16}$$

Additionally, the equations for the immobile phases, attached biomass, and calcite are,

$$\varrho_k\frac{\partial\phi_k}{\partial t} = q^k; \qquad k\in\{\mathrm{f},\mathrm{c}\}. \tag{17}$$

2.4. Sources and Sinks

[24] The sources and sinks given in equations (14)–(17) accounting for reactions (urea hydrolysis, precipitation, dissolution) and bacterial activity are described in detail in the following [cf. *Ebigbo et al.*, 2010]:

[25] Suspended and attached biomass:

$$q^{\mathrm{b}} = r_{\mathrm{g}}^{\mathrm{b}} - r_{\mathrm{b}}^{\mathrm{b}} - r_{\mathrm{a}} + r_{\mathrm{d}} \tag{18}$$

and

$$q^{\mathrm{f}} = r_{\mathrm{g}}^{\mathrm{f}} - r_{\mathrm{b}}^{\mathrm{f}} + r_{\mathrm{a}} - r_{\mathrm{d}}, \tag{19}$$

where $r_{\mathrm{g}}^{\mathrm{b}}$ and $r_{\mathrm{g}}^{\mathrm{f}}$ are growth rates for suspended and attached biomass, respectively; $r_{\mathrm{b}}^{\mathrm{b}}$ and $r_{\mathrm{b}}^{\mathrm{f}}$ are the corresponding decay rates; and r_{a} and r_{d} are the rates of attachment to and detachment from the biofilm, respectively [e.g., *Taylor and Jaffé*, 1990],

$$r_{\mathrm{g}}^{\mathrm{b}} = \mu\phi S_{\mathrm{w}} C_{\mathrm{w}}^{\mathrm{b}}, \tag{20}$$

$$r_{\mathrm{g}}^{\mathrm{f}} = \mu\phi_{\mathrm{f}}\varrho_{\mathrm{f}}. \tag{21}$$

The growth coefficient μ is calculated with double-Monod kinetics [e.g., *Rockhold et al.*, 2004],

$$\mu = k_\mu\frac{C_{\mathrm{w}}^{\mathrm{s}}}{K_{\mathrm{s}} + C_{\mathrm{w}}^{\mathrm{s}}}\cdot\frac{C_{\mathrm{w}}^{\mathrm{e}}}{K_{\mathrm{e}} + C_{\mathrm{w}}^{\mathrm{e}}}. \tag{22}$$

Here k_μ is the maximum substrate utilization rate, and K_{s} and K_{e} are half-saturation coefficients. Decay rates are calculated as first-order relationships with respect to live-cell concentrations,

$$r_{\mathrm{b}}^{\mathrm{b}} = b_{\mathrm{b}}\phi S_{\mathrm{w}} C_{\mathrm{w}}^{\mathrm{b}}, \tag{23}$$

$$r_{\mathrm{b}}^{\mathrm{f}} = b_{\mathrm{f}}\phi_{\mathrm{f}}\varrho_{\mathrm{f}}, \tag{24}$$

where b_{b} and b_{f} are decay coefficients. They comprise constant endogenous decay b_0 and process-dependent decay b^κ ($\kappa\in$ b, f). For the suspended biomass, b^{b} is assumed to be primarily dependent on pH. Since *Sporosarcina pasteurii* is an alkaliphile, only low pH conditions due to high CO_2 concentrations in water are taken to be harmful to the bacterial cells. In addition, it is assumed that the biofilm bacteria are protected from the adverse effects of CO_2. This assumption is supported by the findings of *Mitchell et al.* [2008] in which they propose mechanisms which contribute to the protective nature of the biofilm including mass transfer resistance offered by the biofilm structure and immobilization of CO_2 molecules due to their interaction with the extracellular polymers of the biofilm. Thus, the following decay relationship is chosen [*Kim et al.*, 2000]:

$$b^{\mathrm{b}} = b_0\left(1 + \frac{m_{\mathrm{H}^+}^2}{K_{\mathrm{pH}}}\right), \tag{25}$$

where K_{pH} is an empirical constant.

[26] Precipitation of calcite occurs mainly in and on the biofilm [*Zhang and Klapper*, 2010; *Schultz et al.*, 2011]. This can lead to inactivation of bacterial cells embedded in the biofilm, either by disruption when a calcite nucleus develops within a cell or due to a coating of the cells by the calcite (which effectively leads to inactivation) [*De Muynck et al.*, 2010b; *Whiffin et al.*, 2007; *Parks*, 2009; *Dupraz et al.*, 2009a]. Thus, b^{f} is a function of the calcite precipitation rate:

$$b^{\mathrm{f}} = b_0 + \frac{r_{\mathrm{prec}}M_{\mathrm{CaCO_3}}}{\varrho_{\mathrm{c}}(\phi_0 - \phi_{\mathrm{c}})}. \tag{26}$$

Equation (26) assumes that the rate of inactivation due to precipitation is inversely proportional to the free space available for precipitation, $\phi_0 - \phi_{\mathrm{c}}$.

[27] As in the work of *Ebigbo et al.* [2010], attachment and detachment rates are calculated as follows:

$$r_{\mathrm{a}} = k_{\mathrm{a}}\phi S_{\mathrm{w}} C_{\mathrm{w}}^{\mathrm{b}}, \tag{27}$$

$$r_{\mathrm{d}} = k_{\mathrm{d}}\phi_{\mathrm{f}}\varrho_{\mathrm{f}}. \tag{28}$$

The attachment [cf. *Taylor and Jaffé*, 1990] and detachment [cf. *Rittmann*, 1982; *Speitel and DiGiano*, 1987] coefficients are given by,

$$k_{\mathrm{a}} = c_{\mathrm{a},1}\phi_{\mathrm{f}} + c_{\mathrm{a},2}, \tag{29}$$

$$k_{\mathrm{d}} = c_{\mathrm{d},1}(\phi S_{\mathrm{w}}|\nabla p_{\mathrm{w}} - \varrho_{\mathrm{w}}\mathbf{g}|)^{0.58} + c_{\mathrm{d},2}\mu. \tag{30}$$

The parameters $c_{\mathrm{a},1}$, $c_{\mathrm{a},2}$, and $c_{\mathrm{d},1}$ are all constants [cf. *Taylor and Jaffé*, 1990; *Ebigbo et al.*, 2010], p is fluid-phase pressure, and $\mathbf{g}$ is the gravity vector. *Speitel and DiGiano* [1987] fit the value of $c_{\mathrm{d},2} = 0.665$, whereas *Ebigbo et al.* [2010] obtained a better fit in their model with $c_{\mathrm{d},2} = 6\phi_{\mathrm{f}}$. In this model, better results were obtained with an expression similar to the latter approach. However, since it is required that $0 \le c_{\mathrm{d},2} \le 1$ and that the influence of reduced porespace due to precipitation needs to be included,

$$c_{\mathrm{d},2} = \frac{\phi_{\mathrm{f}}}{\phi_0 - \phi_{\mathrm{c}}}, \tag{31}$$

was used to calculate $c_{\mathrm{d},2}$.

Substrate:

$$q^{\mathrm{s}} = -(r_{\mathrm{g}}^{\mathrm{b}} + r_{\mathrm{g}}^{\mathrm{f}})/Y \tag{32}$$

where Y is the yield coefficient.

Electron acceptor (oxygen):

$$q^{e} = -F \times (r_{g}^{b} + r_{g}^{f})/Y. \quad (33)$$

The coefficient F quantifies the amount of oxygen consumed per unit mass of substrate [*Murphy and Ginn*, 2000].

Urea:

$$q^{u} = -r_{urea} M_{urea}. \quad (34)$$

Ammonia:

$$q^{a} = 2 r_{urea} M_{NH_3}. \quad (35)$$

Calcite:

$$q^{c} = (r_{prec} - r_{diss}) M_{CaCO_3}. \quad (36)$$

Calcium:

$$q^{Ca^{2+}} = (r_{diss} - r_{prec}) M_{Ca^{2+}}. \quad (37)$$

CO_2:

$$q^{CO_2} = (r_{diss} - r_{prec} + r_{urea}) M_{CO_2}. \quad (38)$$

Water, sodium, and chloride:

$$q^{w} = q^{Na^{+}} = q^{Cl^{-}} = 0. \quad (39)$$

2.5. Charge Balance

[28] With the charge balance equation, it is possible to calculate pH,

$$\sum_{i} z_i m_i = 0, \quad (40)$$

where z_i is the charge of the ion i.

2.6. Numerical Model

[29] Some supplementary equations (Appendix A) are required to complete the description of the model. The mass balance equations form a system of 10 partial (equations (14)–(16)) and two ordinary (equation (17)) differential equations. These are implemented, as outlined by *Ebigbo et al.* [2010], in MUFTE-UG using a vertex-centered finite-volume scheme and a fully implicit time discretization.

[30] Depending on the conditions at hand, the sources and sinks, which arise from the chemical and biological reactions, can impose a very strong coupling on the set of equations. In addition, constitutive relationships such as the permeability-porosity function augment this coupling and increase the nonlinear character of the system. Hence, an efficient numerical solution is challenging.

[31] Time-step sizes are automatically adapted to the rate of convergence that depends on the rate at which the processes occur. The process which has the highest influence on time-step size in this model is the rate of calcite precipitation. High-saturation states can lead to very fast precipitation events which, of course, reduce the time step size. In the simulations conducted in this study, the time step sizes ranged from several seconds to several hours.

[32] More information on MUFTE-UG is available in the work of *Assteerawatt et al.* [2005] and *Helmig et al.* [1998].

3. Experiments: Saturated Flow Through Sand-Packed Columns

[33] Laboratory experiments involving saturated flow through sand-packed columns were carried out to optimize the precipitation process and validate part of the numerical model.

[34] As previously described by *Cunningham et al.* [2011], vertically positioned columns (61 cm in length, 2.54 cm in diameter) were packed with 40-mesh (0.5 mm effective filtration size) quartz sand (Unimin Corporation, Emmet, ID) under water to minimize air inclusions. Columns were disinfected and rinsed by injecting two pore volumes followed by 30-min stagnation periods of each of the four following solutions:

[35] 1% bleach (Clorox, Oakland, Calif.) v/v and 3.5% Tween 80 (Acros, N. J.) w/v solution;

[36] 10% w/v NaCl (Fisher, Fair Lawn, N. J.) solution;

[37] 1.26% w/v sodium thiosulfate (Fisher, Fair Lawn, N. J.) solution; and

[38] 4.10% w/v ammonium chloride (Fisher, Fair Lawn, N. J.) solution.

[39] Cultures of *Sporosarcina pasteurii* were grown overnight from a frozen stock culture and washed via centrifugation and resuspension in fresh sterile medium prior to injection into the column in up-flow configuration. A cell-attachment period (no flow) of ~6 h was followed by 18 h of pumping growth medium to develop biofilm. After biofilm establishment and an overnight delay, two pore volumes of calcium-rich (1.25 M calcium) growth medium were injected to initiate biomineralization. The columns were then allowed to remain static for 24 h (biomineralization stage). For columns 2–4, calcium-rich medium from the first 7.6 cm of the columns was displaced immediately after injection with calcium-free medium to minimize injectivity reduction near the injection point. Between biomineralizing stages, the columns were flushed with two pore volumes of calcium- and urea-free medium to restore a low saturation state. Periodically, throughout the experiments, the biofilm was resuscitated by injecting at least two pore volumes of fresh growth medium without calcium. Flow rates were controlled by a Masterflex (model 7553-70) pump and controller (Cole Parmer, Vernon Hills, Ill.). The filling and flushing strategy for all four columns is described in Table 1. The experiments were terminated when the systems' pressure limits were reached. However, column 4 was terminated when as much calcium had been injected as for columns 2 and 3.

[40] Growth medium was prepared by mixing 3 g of Difco Nutrient Broth (BD, Sparks, Md.), 20 g of urea (Fisher, Fair Lawn, N. J.), 10 g of ammonium chloride (Fisher, Fair Lawn, N. J.), and 185 g of calcium chloride dihydrate (not included in calcium-free growth medium) (Acros, N. J.) and stirring continuously until dissolved in

Table 1. Injection Strategy and Physical Parameters for Each Column Experiment

Column	Biomass Concentration of Inoculum[a] (cfu mL^{-1})	Ca^{2+}-Rich-Medium Pulses	Mass of Total Ca^{2+} Injected (g)	Resuscitation Events	Average Flow Rate (mL s^{-1})	Rinse Influent Region
1	4.0×10^9	35	303.4	15	0.167	no
2	1.1×10^8	20	130.3	10	0.150	yes
3	6.5×10^8	11	83.3	4	0.155	yes
4	1.3×10^7	22	135.2	9	0.155	yes

[a]cfu: colony-forming units.

1 L of nanopure water. As necessary, the pH of the medium was adjusted to between 6.0 and 6.3 (the final pH of calcium-rich medium was 5.4–5.6).

3.1. Monitoring and Sampling Methods

[41] Column effluent was collected and monitored for ammonium and residual calcium concentration after each biomineralization stage. A portion of the effluent sample was filtered using a 0.2 μm SFCA Corning syringe filter (Corning Incorporated, N. Y.) and analyzed with a modified Nessler assay for ammonium production. The unfiltered remainder of the effluent sample was used to monitor pH. The details are described in Appendix B.

[42] At the termination of the experiment, each column was destructively sampled by cutting it into eight 7.6 cm sections and digesting triplicate portions of each section's sand contents with 10% trace-metal-grade nitric acid (Fisher, Fair Lawn, N. J.). Calcium analysis was performed on an Agilent 7500 ICP-MS after a 1:5000 or 1:10,000 dilution in 5% trace-metal-grade nitric acid (Fisher, Fair Lawn, N. J.) and compared with certified standards (Agilent Technologies, Environmental Calibration Standard 5183–4688) to estimate the total $CaCO_3$ mineral per mass of sand.

[43] Additionally, images and elemental maps were acquired using the Zeiss Supra 55VP scanning electron microscope located in the Imaging and Chemical Analysis Laboratory at Montana State University. $CaCO_3$ precipitates on sand samples were air-dried and sputter coated with iridium. High-resolution images were taken at 1.0 kV at a working distance of 4.0 mm. Elemental analysis with energy-dispersive X-ray spectroscopy (EDS) was performed at ~20 kV and a working distance of 15 mm.

3.2. Results and Discussion

3.2.1. Residual-Effluent Analysis

[44] $CaCO_3$ precipitation may inactivate microorganisms or create nutrient-diffusion limitations [*De Muynck et al.*, 2010b; *Whiffin et al.*, 2007; *Parks*, 2009; *Dupraz et al.*, 2009a], leading to reduced ureolysis and subsequently less biomineralization. It has also been hypothesized that larger carbonate crystals, less likely to redissolve, are produced when greater bacterial concentrations are present during ureolysis [*Mitchell and Ferris*, 2006]. As such, the biofilm was periodically resuscitated by injecting at least two pore volumes of fresh growth medium without calcium to stimulate the recovery of bacterial populations after precipitation events [*Dupraz et al.*, 2009b]. Both residual-effluent populations and NH_4^+ concentrations (an indication of ureolysis) are greater directly after the biofilm resuscitation events, while these parameters were observed to decrease during active biomineralization periods (Figure 5).

[45] Directly after resuscitation events, effluent pH was restored to above 9 and the NH_4^+ concentrations rose to above 12 g L^{-1}, while during active biomineralizing periods, the pH averaged 6.9 and NH_4^+ concentrations dropped as low as 5.1 g L^{-1}.

3.2.2. Distribution of $CaCO_3$ Deposition

[46] Unlike columns 2–4, column 1 did not employ a calcium-medium-displacement strategy for the injection region. As described previously and observed by other researchers [*Whiffin et al.*, 2007; *Achal et al.*, 2009a;

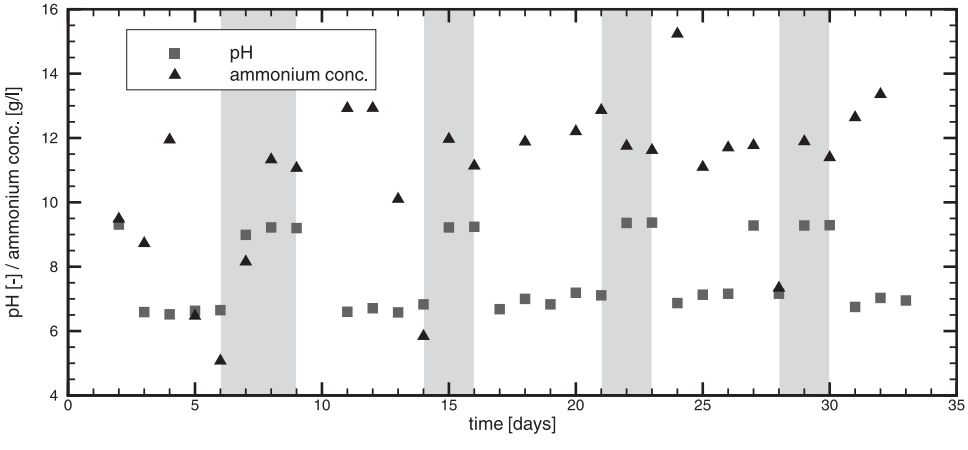

Figure 5. Effluent NH_4^+ concentration and pH data from column 4. Gray areas indicate resuscitation periods. Although not presented here, similar results were observed for the other columns. Note that the injected medium contained 3.4 g L^{-1} of NH_4^+.

Cunningham et al., 2011; *Barkouki et al.*, 2011], higher $CaCO_3$ concentrations per mass of sand were observed in column 1 in the first section near the injection point. Concerns regarding locally reduced injectivity near the injection point of the column [*Whiffin et al.*, 2007; *Fujita et al.*, 2008; *Cunningham et al.*, 2009] led to a modified injection strategy (used for columns 2–4) which involved rinsing Ca^{2+}-rich medium from the influent area before significant ureolysis, and thus $CaCO_3$ precipitation could occur. Favorable results of homogeneous $CaCO_3$ distribution were achieved for columns 2–4 as shown in Figures 6–8. The average $CaCO_3$ contents from each column study are summarized in Table 2. To obtain ϕ_c, the ICP-MS results were converted assuming $\varrho_c = 2710$ g L^{-1} and $\phi_0 = 0.4$, in order to make direct comparisons to the model output results.

4. Model Validation

[47] The numerical model was calibrated using the experimental data for ϕ_c of the first two experiments (i.e., columns 1 and 2) in Table 2. The columns are idealized as 80 cm one-dimensional reactors, purposefully longer than the length of the experimental column (61 cm) to reduce the effect of the boundary conditions at the effluent on the simulations.

[48] The initial conditions were:

[49] 1. $p_w = 1.01325$ bar at the top of the column (effluent) and a hydrostatic pressure profile in the rest of the column;

[50] 2. $X_w^{CO_2} = 5.8 \times 10^{-7}$ g/g (i.e., 5.8×10^{-4} g L^{-1});

[51] 3. $C_w^s = 3$ g L^{-1};

[52] 4. $C_w^e = 0.008$ g L^{-1};

[53] 5. NH_4Cl concentration (from which C_w^a and C_w^{Cl} can be calculated): 10 g L^{-1};

[54] 6. C_w^{Na} is adjusted such that the pH of the solution matches the experimental value, i.e., 6.2. All other components are not present initially.

[55] Flux boundary conditions were used at the inlet for all components. The water-inflow velocity was chosen to match those of the experiments (see Table 1). The fluxes of the dissolved/suspended components depended on the composition of the injected solution. Calcium-free solutions were identical to the solution initially present in the column. Additionally, the flux of $NaCl_2$ during the injection of the calcium-rich solution was chosen such that it corresponded to a $NaCl_2$ concentration of 139.7 g L^{-1} (which corresponds to 185 g L^{-1} of $CaCl_2 \cdot H_2O$), and that of Na^+ such that the pH equals 5.4 (no significant dissolution of calcite is expected due to the high calcium concentrations).

[56] Column inoculation was simulated by setting a biomass flux for 15 min at the inlet corresponding to the bacterial concentrations listed in Table 1. It is assumed here that the dry cell weight is 2.5×10^{-13}g/cfu [e.g., *Norland et al.*, 1987].

[57] After the biofilm was established ($t \approx 2$ d), the strategy was generally to inject two pore volumes each of the calcium-free and calcium-rich solutions, a small amount (equivalent to the pore volume of the first 7.6 cm of the porous-medium column) of calcium-free solution (not for column 1) to minimize precipitation at the inlet, and then shutting off the injection (no flow) for ~24 h. This cycle was repeated for the duration of each experiment. In addition, periodic resuscitation (injection of at least two pore volumes of calcium-free growth medium) was simulated as appropriate. The various injections and rest periods carried out in the different experiments are reproduced by the model. It should be noted that, in the experiments, the columns are not geomechanically confined. Volume changes, which may be caused by calcite precipitation, are not accounted for by the model. At the effluent, all boundary conditions are Dirichlet and set to zero, except the pressure which is atmospheric.

[58] The parameters used for the simulations are shown in Table 3. Six parameters were fitted, including ϱ_f, k_μ, $c_{a,1}$, $c_{a,2}$, k_{ub}, and n_{ub}. This was done manually by varying these parameters within plausible ranges of validity (see footnotes in Table 3) to match the calcite distribution along the columns in the experiments.

[59] Figure 6 shows the results of the simulation for the columns used for model calibration. The calibrated model predicted ϕ_c for columns 3 and 4 with little error: the

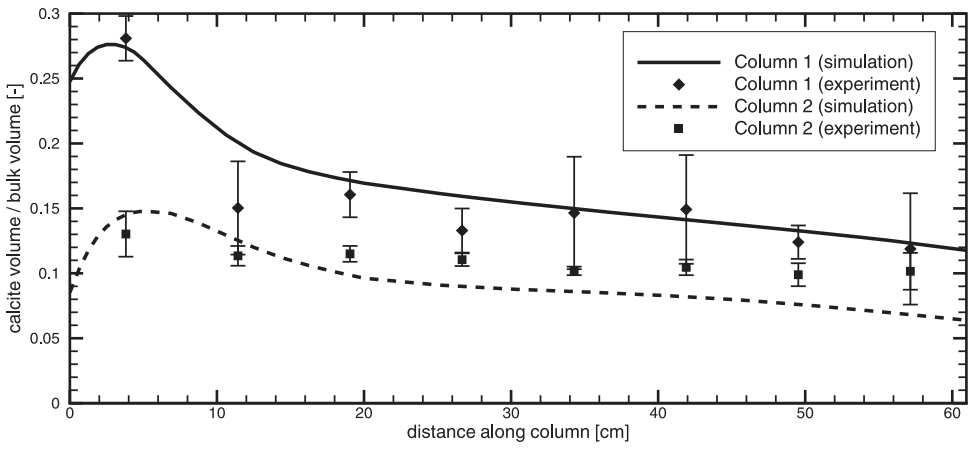

Figure 6. Calcite volume per bulk volume ϕ_c. Columns 1 (at $t = 58$ d) and 2 (at $t = 35$ d) were used for the calibration of the model as shown in Table 3. Six model parameters were fitted here. The symbols show experimental data with standard deviations, and lines are simulation results. In the simulations, calcite precipitation is lower directly at the inlet as a result of the high ionic strength caused by the injection of Ca^{2+} which reduces the activity of CO_3^{2-} as shown in Figure 2.

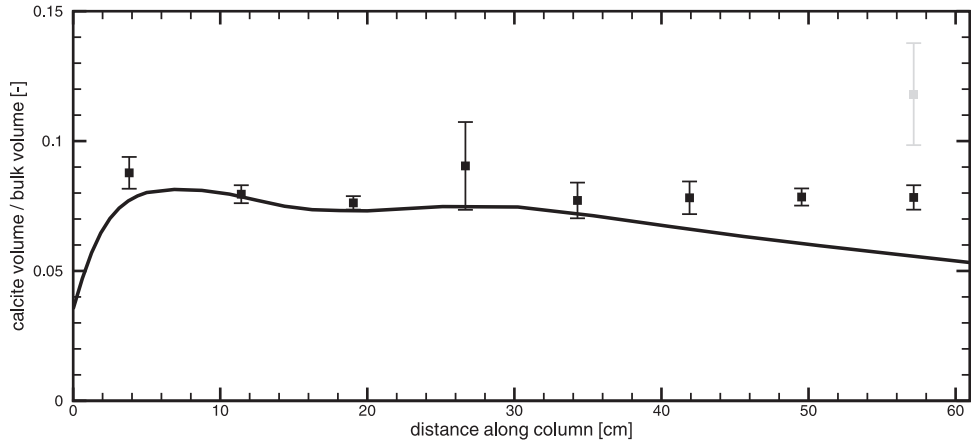

Figure 7. Calcite volume per bulk volume ϕ_c for column 3 at $t = 17$ d. Results of predictive modeling of the column 3 experiment using the calibrated set of parameters from columns 1 and 2. Symbols show experimental data, and lines are simulation results. Model predictions are in good agreement with experimental results except toward the outlet of the column. It is worth noting that in the first evaluation of this experiment, the amount of calcite estimated in the last column section was significantly higher (gray symbol). This was attributed to an inclusion of calcite precipitates from the effluent tubing in the calculation of ϕ_c. The amount of calcite in this section was subsequently re-evaluated separately, and the resulting value is shown in black.

root-mean-square errors were 0.0046 and 0.0032, respectively. However, in column 3 (Figure 7), the results differ slightly from the experimental data toward the effluent. These differences, particularly toward the effluent, could be the result of an artifact in the experiments of calcium carbonate precipitating in the nonporous-medium-containing effluent section and settling onto and possibly into the effluent section. Additionally, increased bacterial (and thus ureolytic) activity could be due to diffusion of oxygen through the silicon tubing in the effluent leading to increased microbial concentrations, and thus precipitation.

[60] In addition to the calcite distribution along the column, the modeling results are compared to the pH of the effluent samples taken during the experiments. The samples were taken after mineralization phases, 7 min after flow was restarted. While the pH data was not used in the model calibration, good correlation between the model and experimental results were achieved (Figure 9).

[61] However, the experiments generally show a stronger variation of pH than the model. This may indicate an overestimation of the buffering capacity of the carbonate mineral by the model, i.e., an overestimation of the rates of precipitation and dissolution. Data for precipitation and dissolution rates were taken from studies without the interference of microorganisms capable of forming biofilms. It is possible that the presence of the biofilm reduces these rates. This may also be a source of error for the model prediction of the amount of Ca^{2+} precipitates, particularly toward the effluent of the columns.

[62] The effect of the injection strategy used for columns 2–4 on the saturation state Ω of calcite and hence on calcite precipitation within the column is illustrated in Figure 10.

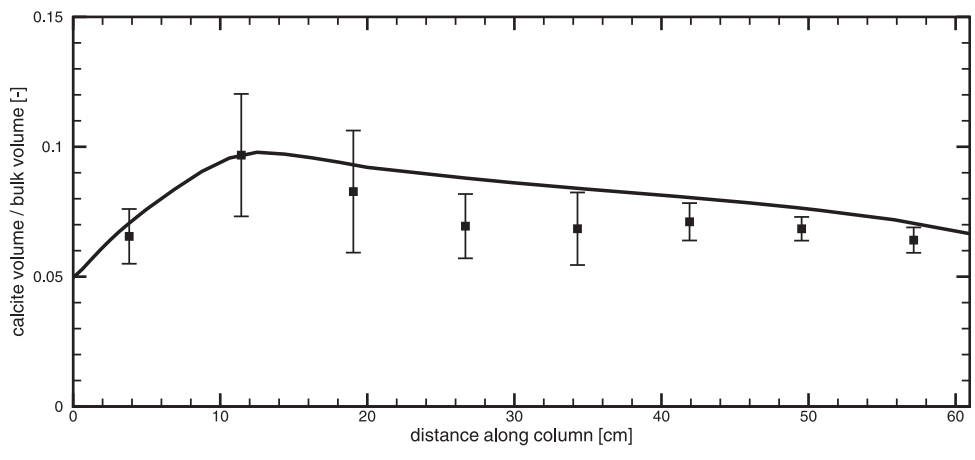

Figure 8. Calcite volume per bulk volume ϕ_c for column 4 at $t = 34$ d. Results of predictive modeling of column 4 experiment using the calibrated set of parameters from columns 1 and 2. Symbols show experimental data, and lines are simulation results. Model predictions are in good agreement with the experiment.

Table 2. Results of Sand-Packed Column Experiments[a]

	Section							
Column	1	2	3	4	5	6	7	8
1	479 ± 29	256 ± 61	274 ± 30	227 ± 29	250 ± 74	254 ± 71	211 ± 22	202 ± 73
2	222 ± 30	193 ± 13	196 ± 10	188 ± 80	174 ± 60	178 ± 10	169 ± 15	173 ± 24
3	150 ± 10	136 ± 60	130 ± 40	154 ± 29	132 ± 12	133 ± 11	134 ± 60	201 ± 34
4	112 ± 18	165 ± 40	141 ± 40	118 ± 21	117 ± 24	121 ± 12	117 ± 80	109 ± 80

[a]Average concentration per column section ±1 SD [mg $CaCO_3$/g sand].

It can be seen that the injection of a small amount of calcium-free medium into the column just before the biomineralization phase leads to a reduction of Ω next to the injection point. The figure also shows that the biomass does not distribute uniformly within the column, but accumulates mostly at the inlet due to the availability of oxygen at the inlet.

5. Sensitivity Study

[63] In order to gain some insight into the importance of the uncertain parameters fitted in section 4, a sensitivity study was conducted. All six parameters (ϱ_f, k_μ, $c_{a,1}$, $c_{a,2}$, k_{ub}, and n_{ub}) were varied within a given range to determine their effects on the error as compared to the experimental measurements. It must be noted, however, that the

Table 3. Parameters Used for Simulation of Experiments[a]

Parameter	Value	Comment/source	Brief description
ϕ_0	0.4	Measured	Initial porosity
ϕ_{crit}	0	Estimated[b]	Critical porosity
	2.30×10^{-8} dm^2	Columns 1 and 2, measured	Initial permeabilities
K_0	1.79×10^{-8} dm^2	Column 3, measured	Initial permeabilities
	1.82×10^{-8} dm^2	Column 4, measured	Initial permeabilities
ϱ_c	2710 g L^{-1}	–	Calcite density
ϱ_f	10 g L^{-1}	**Fitted**[c]	Biofilm density (dry)
D_w	10^{-7} dm^2 s^{-1}	–	Molecular diffusion
α_L	0.25 dm	Estimated from *Frippiat et al.* [2008]	Long. dispersivity
$A_{sw,0}$	500 dm^2 dm^{-3}	Estimated from ϕ_0	Specific surface areas
a_c	2000 dm^2 dm^{-3}	Estimated[d]	Specific surface areas
k_{prec}	1.5×10^{-12} mol/(dm^2 s)	*Zhong and Mucci* [1989]	Precip. parameters in equation (5)
n_p	3.27	*Zhong and Mucci* [1989]	Precip. parameters in equation (5)
$k_{diss,1}$	8.9×10^{-3} Kg$_{H_2O}$/(dm^{2}s)	*Chou et al.* [1989]	Dissolution parameters in equation (7)
$k_{diss,2}$	6.5×10^{-9} mol/(dm^2 s)	*Chou et al.* [1989]	Dissolution parameters in equation (7)
n_d	1	*Flukiger and Bernard* [2009]	Dissolution parameters in equation (7)
k_μ	2.89×10^{-5} s^{-1} (2.5d^{-1})	**Fitted**[e]	Substrate utilization
K_s	7.99×10^{-4} g L^{-1}	*Taylor and Jaffé* [1990]	Half-saturation constants
K_e	2×10^{-5} g L^{-1}	*Hao et al.* [1983]	Half-saturation constants
Y	0.5	*Seto and Alexander* [1985]	yield coefficient
F	0.5	*Mateles* [1971]	O_2 consumption
b_0	3.18×10^{-7} s^{-1} (0.0275 d^{-1})	*Taylor and Jaffé* [1990]	Decay coefficient
K_{pH}	6.15×10^{-10}(mol/kg$_{H_2O}$)^2	*Kim and Fogler* [2000]	Decay parameter in equation (25)
$c_{a,1}$	0.0443 s^{-1} (3831 d^{-1})	**Fitted**[f]	Attachment parameters Attachment parameters
$c_{a,2}$	9.19×10^{-4} s^{-1} (79.38 d^{-1})	**Fitted**[f]	Attachment parameters
$c_{d,1}$	2.89×10^{-8} s^{-1} 2.5×10^{-3} d^{-1}	*Ebigbo et al.* [2010]	Detachment parameter
k	0.0417 mol/(g s) (2500μ mol/(mg min))	*Krajewska* [2009]	Rate of ureolysis
K_u	0.0173 mol/kg$_{H_2O}$	*Krajewska* [2009]	Parameters in equation (1) for calculation of ureolysis rate
$K_{EU,1}$	7.57×10^{-7} mol/kg$_{H_2O}$	*Fidaleo and Lavecchia* [2003]	Parameters in equation (1) for calculation of ureolysis rate
$K_{EU,2}$	1.27×10^{-8} mol/kg$_{H_2O}$	*Fidaleo and Lavecchia* [2003]	Parameters in equation (1) for calculation of ureolysis rate
$K_{NH_4^+}$	0.0122 mol/kg$_{H_2O}$	*Fidaleo and Lavecchia* [2003]	Parameters in equation (1) for calculation of ureolysis rate
k_{ub}	0.11	**Fitted**	Parameters in equation (3)
n_{ub}	1.5	**Fitted**	Parameters in equation (3)
T	25°C	Constant	Temperature

[a]Fitting is done using columns 1 and 2. Fitted parameters are highlighted in bold.

[b]The relatively large values of ϕ_c (~0.3) at the influent of column 1 suggest that ϕ_{crit} is lower than the range of porosities achieved in these experiments.

[c]Literature values for ϱ_f include (in g L^{-1}) 14–91 [*Melo*, 2005], 2.5 and 3 [*Taylor and Jaffé*, 1990], 29.3 and 38.4 [*Zhang and Bishop*, 1994], 34–76 [*Tanyolac and Beyenal*, 1997].

[d]Estimated as $a_c \approx \frac{3}{r}$ (assuming the "effective" radius of a calcite crystal $r = 150\,\mu$m). The results of these simulations were not sensitive to a_c.

[e]Literature values for k_μ vary with bacterial strain and environmental conditions, e.g., 2.6 – 6.5 d^{-1} [*Hao et al.*, 1983], 7.7 d^{-1} [*Taylor and Jaffé*, 1990].

[f]These values are lower but not very different from those of *Taylor and Jaffé* [1990] where $c_{a,1} = 6810$ d^{-1} and $c_{a,2} = 635$ d^{-1}.

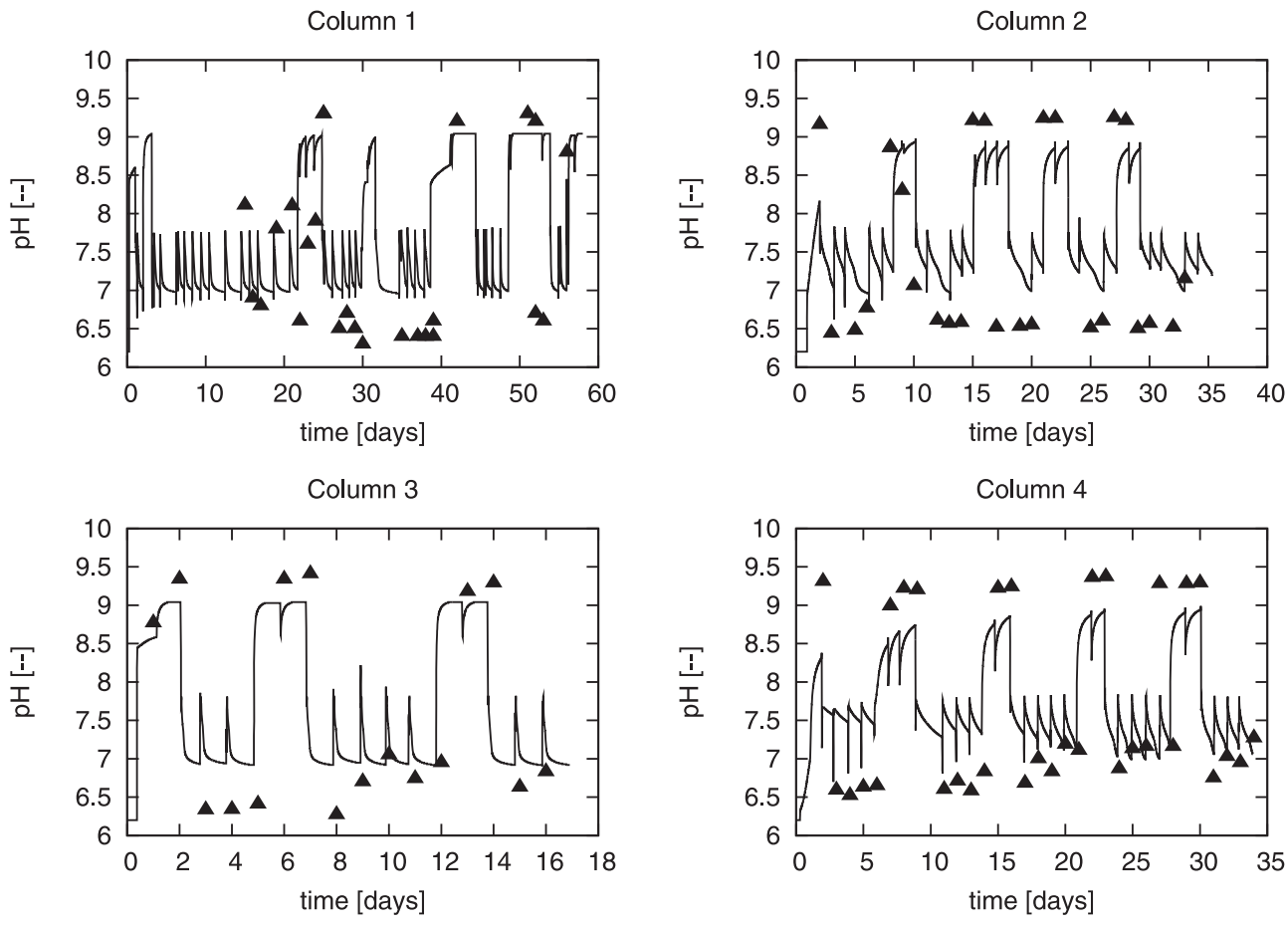

Figure 9. Comparison of effluent pH over time resulting from the experimental procedure for all four experiments. Continuous lines are model predictions, while the symbols are the measurements.

parameters are varied individually. A detailed investigation of parameter correlations is beyond the scope of this study, although it might give further valuable insight. Nonetheless, the main sources of uncertainty for the model with respect to parameterization can be shown with this study.

[64] For each parameter, a lower and an upper limit were defined. For the substrate utilization rate k_μ and the biofilm density ϱ_f, these can be determined from literature (see the footnotes in Table 3). However, for the other parameters, the lower and upper limits are more difficult to determine. As such, they were approximated by the variation of the fitted values given in Table 3 by approximately an order of magnitude in both directions (see Table 4). Intermediate parameter values, defined as either half or double the fitted

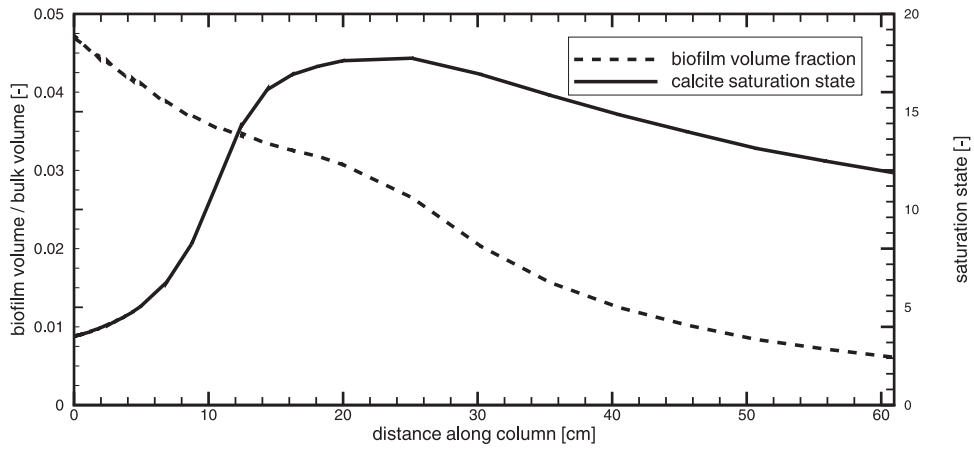

Figure 10. Results of simulation for column 4 showing the calcite saturation state Ω and biofilm volume fraction along the column length (at $t = 33$ d) during the final biomineralization phase.

Table 4. Variation of Parameters for Sensitivity Study

	ϱ_f[g L^{-1}]	k_μ[1 d^{-1}]	$c_{a,1}$[1 d^{-1}]	$c_{a,2}$[1 d^{-1}]	k_{ub}	n_{ub}
Upper limit	50	4	40,000	800	1	2.5
Lower limit	5	1	400	8	0.01	0.5
High value	–	–	7662	158.76	0.22	2
Low value	–	–	–	–	0.055	1
Original value	10	2.5	3831	79.38	0.11	1.5

value, are referred to as low and high values, respectively (Table 4). Intermediate-value simulations were carried out only for the parameters to which the system is most sensitive, as shown in Table 4.

[65] The results of the sensitivity study as shown in Figure 11 clearly demonstrate that for this setup, the model is most sensitive to the proportionality factor k_{ub}. A quantification of this parameter experimentally would significantly reduce the model uncertainty.

6. Simulations With Two Fluid Phases

[66] The effect of dense-phase CO_2 on the mineral barrier is the focus of current research by the authors. The numerical model is a useful tool with which several processes can be investigated and new experiments can be designed. As an example, in this section, possible effects of free-phase CO_2 on carbonate precipitates are investigated with the help of the numerical model.

[67] A simple simulation is shown here in which CO_2 is injected into a column in which a given amount of calcite ($\phi_c = 0.1$) and biofilm ($\phi_f = 0.05$) are initially present and uniformly distributed. The other initial and boundary conditions are identical to those of the experiments with saturated flow except pressure which is assumed to be 80 bar.

[68] Two injection scenarios were tested. In both cases, the total injection rate and other parameters were the same as in the column 4 experiment (i.e., 0.155 mL s^{-1}), and a constant mass fraction of water in CO_2 of 1.5×10^{-4} g g^{-1} is assumed (corresponding to the saturation pressure of water in the CO_2 phase at 25°C and 80 bar): injection of pure CO_2 and injection of 90% (by volume) CO_2 (i.e., 0.1395 mL s^{-1}) and 10% water (i.e., 0.0155 mL s^{-1}).

[69] These result in two fluid phases within the column. A simulation time of 3 d is chosen. Two-phase-flow parameters used here include residual water and CO_2 saturations $S_{wr} = 0.1$ and $S_{nr} = 0.05$, pore size-distribution index $\lambda = 2$, entry pressure $p_d = 0.1$ bar (see A4 for the capillary-pressure-saturation and relative-permeability-saturation relations). The molecular diffusion coefficient for the CO_2 phase is approximated with $D_{CO_2} = 10^{-3}$ dm^2 s^{-1}.

[70] As can be seen in Figure 12, the simulations show that:

[71] 1. The injection of pure, dense-phase CO_2 leads to limited calcite dissolution within the column because the dissolution of $CaCO_3$ buffers the pH of the medium, minimizing further dissolution.

[72] 2. The injection of both CO_2 and water leads to relatively fast dissolution. The injected water flushes out resident water reducing the buffering capacity of the calcite. As such, limited success of this technology may be seen with CO_2 injection strategies involving large volumes of simultaneously injected water.

7. Conclusions

[73] 1. Relatively uniform microbially mediated precipitation could be achieved in three of the four experiments involving water-saturated flow through 61 cm, sand-packed columns when near-injection-point calcium-medium displacement strategies were used.

[74] 2. Calcium deposition efficiency may be optimized by balancing biomineralizing periods with bacterial resuscitation events. Long biomineralization periods could lead to inactivation of bacterial cells (due to cell encapsulation),

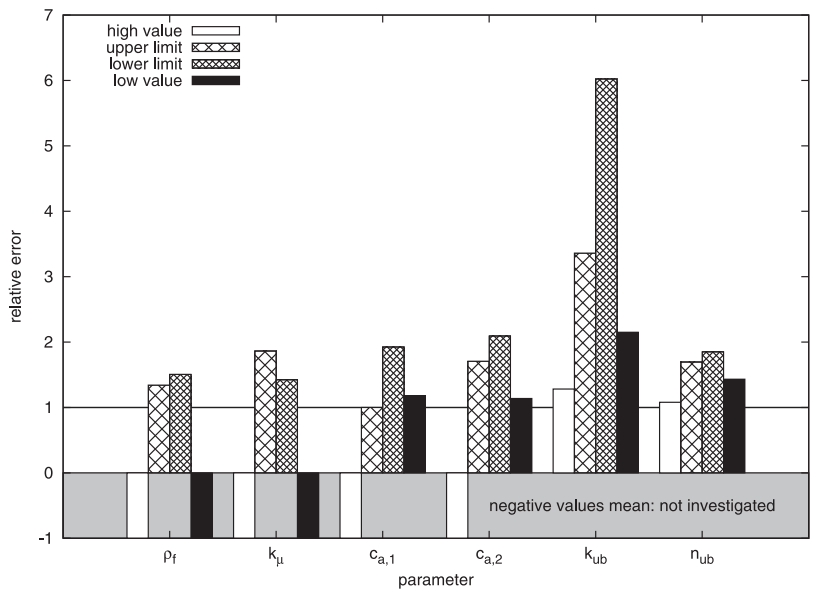

Figure 11. The effect of six parameters on the error made by the numerical model as compared to the experimental data on calcite distribution. The histogram shows error (i.e., total sum of the squared errors for both columns) relative to the error with the calibrated parameters.

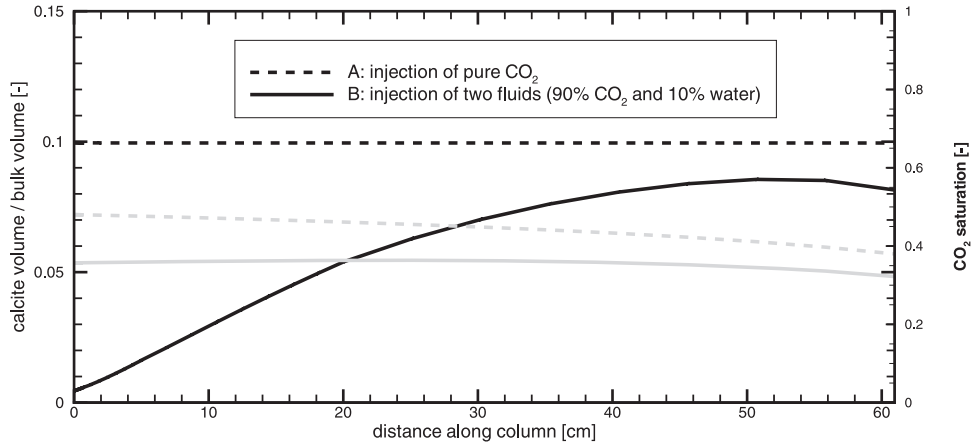

Figure 12. Results of simulations (at $t = 3$ d) showing the effect of pure CO_2 and a CO_2-water mixture on calcite within the sand column. The black lines show the calcite distribution, while the gray lines show the saturation of CO_2.

reduced ureolysis, and, ultimately, reduced calcium deposition efficiency.

[75] 3. A numerical model has been developed, capable of describing microbially induced carbonate precipitation and dissolution in porous media in the presence of water and CO_2 flow.

[76] 4. Part of the numerical model, i.e., for water-saturated flow through sterilized sand, was validated with experimental data for one-dimensional column experiments. It should be noted that a transfer of the model to field scenarios might not be straightforward while focusing on model scale-up is currently ongoing [A. Phillips, et al. (2012), Potential CO_2 leakage reduction through biofilm-induced calcium carbonate precipitation, submitted to *Environmental Science and Technology*, 2012].

8. Outlook

[77] 1. The model can and will be used to optimize injection strategies to achieve a large radius of influence in larger-scale, three-dimensional experiments.

[78] 2. High-pressure, dense-phase-CO_2 experiments will be designed using the model as a predictive tool.

[79] 3. In the future, the two-phase-flow model will be validated with the results of high-pressure laboratory experiments.

[80] 4. The model would also be suitable, with slight modifications, for other applications involving microbially induced $CaCO_3$ precipitation including (but not limited to) strontium coprecipitation as well as soil and dike stabilization.

Appendix A: Supplementary Equations for Description of Model

A1. Changes in Permeability

[81] The porosity of the porous medium can be calculated from ϕ_f, ϕ_c, and the initial porosity ϕ_0,

$$\phi = \phi_0 - \phi_f - \phi_c. \tag{A1}$$

Given porosity, permeability K is calculated using a Kozeny-Carman-type equation [e.g., *Xu et al.*, 2004],

$$\frac{K}{K_0} = \begin{cases} \left(\dfrac{\phi - \phi_{crit}}{\phi_0 - \phi_{crit}}\right)^3 & \text{if } \phi > \phi_{crit} \\ 0 & \text{otherwise} \end{cases}. \tag{A2}$$

The critical porosity ϕ_{crit} is the porosity at which the permeability is zero.

A2. Solubilities

[82] The solubility of CO_2 in the water phase is calculated from *Duan and Sun* [2003] as a function of temperature, pressure, and equivalent salinity. When both phases are present, the concentration of H_2CO_3 is equivalent to the solubility. In the absence of the CO_2 phase, the solubility is the maximum possible concentration of H_2CO_3 in water. For simplicity, X_n^w is assumed to be constant [*Bielinski*, 2006].

[83] Henry's law is used for the calculation of the solubility of oxygen in water (R. Sander, Compilation of Henry's Law constants for inorganic and organic species of potential importance in environmental chemistry (version 3), 1999, available at http://www.henrys-law.org).

A3. Velocity (Darcy Equation)

[84] Velocity is calculated as

$$\mathbf{v}_\alpha = -\frac{k_{r\alpha}(S_\alpha)}{\mu_\alpha} K(\nabla p_\alpha - \varrho_\alpha \mathbf{g}), \tag{A3}$$

k_r is the relative permeability (calculated as a function of saturation using Brooks-and-Corey relationships as done by *Ebigbo et al.* [2010]).

A4. Capillary Pressure

[85] Capillary pressure is the difference between the phase pressures:

$$p_{cap}(Sw) = p_n - p_w\,. \tag{A4}$$

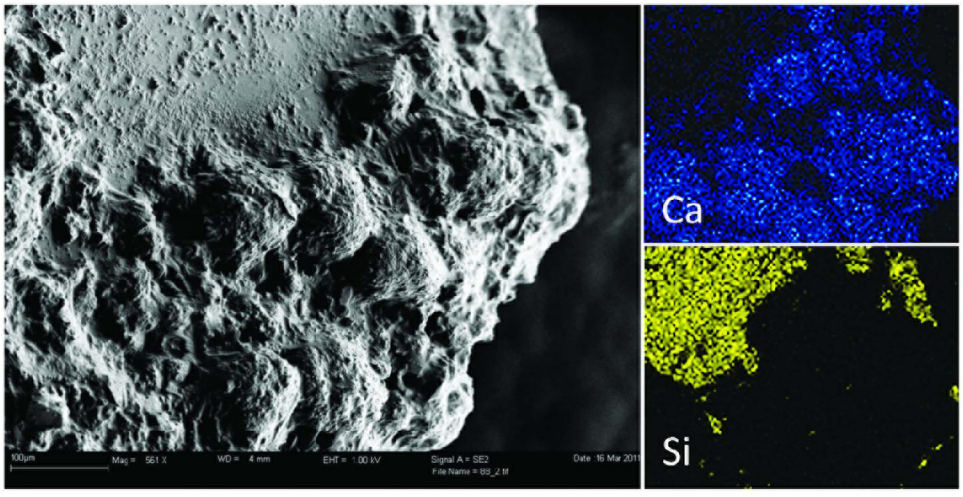

Figure 13. Scanning electron micrograph of $CaCO_3$-crystal structure on sand particle along with EDX elemental maps for calcium and silicon (scale bar: 100 μm).

It is calculated using the relationship of Brooks and Corey [e.g., *Ebigbo et al.*, 2010].

A5. Dispersion

[86] The hydrodynamic dispersion coefficient is calculated as follows [*Bear*, 1979]:

$$\mathbf{D}_\alpha = \underbrace{D_\alpha \tau_\alpha S_\alpha \phi}_{\text{molecular diffusion}} + \underbrace{\alpha_T \mathbf{I} |\hat{\mathbf{v}}_\alpha| + (\alpha_L - \alpha_T) \frac{\hat{\mathbf{v}}_\alpha \otimes \hat{\mathbf{v}}_\alpha}{|\hat{\mathbf{v}}_\alpha|}}_{\text{mechanical dispersion}}, \quad \alpha \in \{w, n\}, \tag{A5}$$

where α_L and α_T are the longitudinal and transverse dispersivities, $\mathbf{I}$ is the unit tensor, D is the molecular diffusion coefficient, the velocity is calculated as $\hat{\mathbf{v}}_\alpha = \mathbf{v}_\alpha / \phi$, and τ is tortuosity calculated as given by *Millington and Quirk* [1961]:

$$\tau_\alpha = \frac{(\phi S_\alpha)^{\frac{7}{3}}}{\phi^2}. \tag{A6}$$

A6. Fluid Properties

[87] CO_2 density is calculated using the equation of state by *Span and Wagner* [1996], and viscosity from *Fenghour et al.* [1998]. The effects of small amounts of water and oxygen in this phase are not accounted for in these calculations.

[88] The density and viscosity of the water phase is calculated as a function of salinity as given by *Batzle and Wang* [1992]. For the calculation of salinity, the NaCl and $NaCl_2$ salts are considered.

Appendix B: Monitoring of Activity in Sand-Packed Columns

[89] During the experiments, the activity in the column was monitored as follows:

[90] 1. Ammonium concentration was determined with a modified Nessler assay; effluent samples were diluted in deionized water and compared to standards made from $(NH_4)_2SO_4$. Each sample and standard (250μL) was added in triplicate to a 96-well microplate (Fisher, Fair Lawn N. J.) to which 3 μL of mineral stabilizer and polyvinyl alcohol, and 10 μL of Nessler reagent (potassium tetraiodomercurate(II)) (Hach, Loveland, Colo.) were added. Ammonium concentration was quantified in the resulting solution after 13 min reaction time via spectrophotometry at 425 nm (Bio-Tek, Synergy HT).

[91] 2. The pH of effluent samples was assessed with a Fisher Scientific pH meter (model 50) equipped with a Corning glass electrode, which was calibrated daily with pH 7 and 10 buffers.

Appendix C: Image and EDX Analysis of Minerals

[92] Figure 13 depicts the surface of sand from a treated column where calcium carbonate crystals were observed in the size range of $10 - 100\,\mu$m. Spot EDX analysis of the crystals confirmed the presence of elemental calcium (data not shown). In addition, EDX elemental mapping revealed calcium in regions where obvious crystals had formed and silica in the region of the base materials (see Figure 13). This result leads to additional support that the formed minerals were calcium carbonate.

Notation

α_L, α_T	Longitudinal and transverse dispersivities [dm]
ϕ	Porosity
ϕ_0	Initial porosity
ϕ_c	Volume fraction of calcite $[l_{calcite}/l_{bulk}]$
ϕ_{crit}	Critical porosity at which $K = 0$
ϕ_f	Volume fraction of biofilm $[l_{biofilm}/l_{bulk}]$
γ	Activity coefficient
μ	Biomass growth coefficient [1 s^{-1}] or [1 d^{-1}]
μ_α	Dynamic fluid-phase viscosity [Pa s] or [g/(dm s)]
λ	Pore size-distribution index
ν_{max}	Maximum specific rate of urea hydrolysis $[mol_{urea}/(g_{urease}\ s)]$

Ω	Calcite saturation state
ϱ	Density [kg m^{-3}] or [g L^{-1}]
τ	Tortuosity
a_c	Specific surface area of calcite grains [dm^2 L^{-1}]
b	Decay coefficient [L s^{-1}] or [L d^{-1}]
b_0	Endogenous decay coefficient [L s^{-1}] or [L d^{-1}]
$c_{a,i}$	Parameters for the calculation of k_a
$c_{d,i}$	Parameters for the calculation of k_d
g	Gravitation vector [ms^{-1}]
k	Specific rate of urea hydrolysis [mol$_{urea}$/(g$_{urease}$ s)]
k_μ	Maximum substrate utilization rate [L s^{-1}] or [L d^{-1}]
k_a	Attachment coefficient [L s^{-1}] or [L d^{-1}]
k_d	Detachment coefficient [L s^{-1}] or [L d^{-1}]
$k_{diss,1}$	Parameter for calculation of r_{diss} [kg$_{H_2O}$/(dm^2 s)]
$k_{diss,2}$	Parameter for calculation of r_{diss} [mol/(dm^2 s)]
k_{prec}	Parameter for calculation of r_{prec} [mol/(dm^2 s)]
k_r	Relative permeability
k_{ub}	Parameter for the calculation of Z_{ub}
m	Molality [mol/kg$_{H_2O}$]
n_d	Parameter for calculation of r_{diss}
n_p	Parameter for calculation of r_{prec}
n_{ub}	Parameter for the calculation of Z_{ub}
p	Phase pressure [Pa] or [bar]
p_{cap}	Capillary pressure [Pa] or [bar]
p_d	Entry pressure [Pa] or [bar]
q	Source/sink [g/(L s)]
r_a	Biomass attachment rate [g/(L s)]
r_b	Biomass decay rate [g/(L s)]
r_d	Biomass detachment rate [g/(L s)]
r_{diss}	Net rate of calcite dissolution [mol/(L s)]
r_g	Biomass growth rate [g/(L s)]
r_{prec}	Net rate of calcite precipitation [mol/(L s)]
r_{urea}	Rate of urea hydrolysis [mol$_{urea}$/(L s)]
v	Darcy flux/velocity [dm s^{-1}]
z	Ionic charge
A_{cw}	Specific surface area between water and calcite [dm^2 L^{-1}]
A_{sw}	Specific surface area between water and solids (i.e., both porous matrix and calcite) [dm^2 L^{-1}]
$A_{sw,0}$	Initial value of A_{sw} [dm^2 L^{-1}]
C	Concentration [g L^{-1}]
D	Hydrodynamic dispersion [dm^2 s^{-1}]
D	Molecular diffusion coefficient [dm^2 s^{-1}]
F	Oxygen consumption per unit mass of substrate
K	Permeability [dm^2]
K_1^*	Apparent dissociation coefficient of H_2CO_3 [mol/kg$_{H_2O}$]
K_2^*	Apparent dissociation coefficient of HCO_3^- [mol/kg$_{H_2O}$]
K_a^*	Apparent dissociation coefficient of NH_4^+ [mol/kg$_{H_2O}$]
$K_{EU,i}$	Dissociation constants for enzyme-urea complex [mol/kg$_{H_2O}$]
$K_{NH_4^+}$	Parameter for inhibition due to NH_4^+ [mol/kg$_{H_2O}$]
K_{pH}	Constant for calculation of pH-dependent decay [(mol/kg$_{H_2O}$)^2]
K_s, K_e	Monod half-saturation constant [g L^{-1}]
K_u	Ureolysis half-saturation constant [mol/kg$_{H_2O}$]
K_{sp}	Calcite solubility product [(mol/kg$_{H_2O}$)^2]
K_w^*	Apparent dissociation coefficient of water [(mol/kg$_{H_2O}$)^2]
M	Molecular mass [g mol^{-1}]
S	Saturation
S_r	Residual saturation
T	Temperature [°C]
X	Mass fraction
Y	Yield coefficient
Z_{ub}	Concentration of urease in porous medium [g L^{-1}]
Subscripts	
c	Calcite
f	Attached biomass/biofilm
n	Nonwetting phase
w	Wetting phase
Superscripts	
a	Ammonia/ammonium
b	Suspended biomass
c	Calcite
Ca^{2+}	Calcium
Cl^-	Chloride
CO_2	Carbon dioxide
e	Electron acceptor/oxygen
f	Biofilm
Na^+	Sodium
s	Growth substrate
u	Urea
w	Water

[93] **Acknowledgments.** This work was carried out within the framework of the International Research Training Group NUPUS funded by the German Research Foundation DFG, the Netherlands Organisation for Scientific Research NWO, and the Norwegian Research Council NRC. Funding for the experimental work was provided by the Zero Emissions Research and Technology (ZERT) program (DOE award DE-FC26-04NT42262), DOE EPSCoR program (DOE award DE-FG02-08ER46527), and the DOE Office of Science, Subsurface Biogeochemical Research Program (SBR), contract DE-FG02-09ER64758. Any opinions, conclusions, findings, or recommendations expressed herein are those of the authors and do not necessarily reflect those of DOE. Also, the authors acknowledge funding for the establishment and operation of the Environmental and Biofilm Mass Spectrometry Facility at Montana State University (MSU) through the Defense University Research Instrumentation Program (DURIP, contract W911NF0510255) and the MSU Thermal Biology Institute from the NASA Exobiology Program (project NAG5-8807). Joshua Stringam is acknowledged for his help in the laboratory and Johannes Hommel for proofreading. The reviewers are also acknowledged for their constructive criticism. The experimental work in this paper was conducted by A. Phillips.

References

Achal, V., A. Mukherjee, P. C. Basu, and M. S. Reddy (2009a), Lactose mother liquor as an alternative nutrient source for microbial concrete production by *Sporosarcina pasteurii*, *J. Ind. Microbiol. Biotechnol.*, *36*(3), 433–438.

Achal, V., A. Mukherjee, P. C. Basu, and M. S. Reddy (2009b), Strain improvement of *Sporosarcina pasteurii* for enhanced urease and calcite production, *J. Ind. Microbiol. Biotechnol.*, *36*(7), 981–988.

Assteerawatt, A., et al. (2005), MUFTE-UG: Structure, applications and numerical methods, *Newsletter, International Groundwater Modeling Centre, Colorado School of Mines*, *23*(2), 10.

Barkouki, T. H., B. C. Martinez, B. M. Mortensen, T. S. Weathers, J. D. DeJong, T. R. Ginn, N. F. Spycher, R. W. Smith, and Y. Fujita (2011), Forward and inverse bio-geochemical modeling of microbially induced calcite precipitation in half-meter column experiments, *Transp. Porous Media*, *90*(1), 23–39.

Batzle, M., and Z. J. Wang (1992), Seismic properties of pore fluids, *Geophysics*, *57*(11), 1396–1408.

Bear, J. (1972), *Dynamics of Fluids in Porous Media*, 784 pp., Elsevier, N. Y.

Bear, J. (1979), *Hydraulics of Groundwater*, 592 pp., McGraw-Hill, London, U. K.

Bell, T. G., M. T. Johnson, T. D. Jickells, and P. S. Liss (2008), Ammonia/ammonium dissociation coefficient in seawater: A significant numerical correction, *Env. Chem.*, *5*(3), 183–186.

Bielinski, A. (2006), Numerical simulation of CO_2 sequestration in geological formations, Ph.D. thesis, Universität Stuttgart, Germany.

Brotherton, J. E., A. Emery, and V. W. Rodwell (1976), Characterization of sand as a support for immobilized enzymes, *Biotechnol. Bioeng.*, *18*(4), 527–543.

Chou, L., R. M. Garrels, and R. Wollast (1989), Comparative study of the kinetics and mechanisms of dissolution of carbonate minerals, *Chem. Geol.*, *78*(3–4), 269–282.

Ciurli, S., C. Marzadori, S. Benini, S. Deiana, and C. Gessa (1996), Urease from the soil bacterium *Bacillus pasteurii*: Immobilization on Ca-polygalacturonate, *Soil Biol. Biochem.*, *28*(6), 811–817.

Class, H., R. Helmig, and P. Bastian (2002), Numerical simulation of non-isothermal multiphase multicomponent processes in porous media. 1. An efficient solution technique, *Adv. Water Resour. 25*, 533–550.

Clegg, S. L., and M. Whitfield (1995), A chemical-model of seawater including dissolved ammonia and the stoichiometric dissociation-constant of ammonia in estuarine water and seawater from $-2°C$ to $40°C$, *Geochim. Cosmochim. Acta*, *59*(12), 2403–2421.

Clement, T. P., B. S. Hooker, and R. S. Skeen (1996), Macroscopic models for predicting changes in saturated porous media properties caused by microbial growth, *Ground Water*, *34*(5), 934–942.

Compton, R. G., K. L. Pritchard, and P. R. Unwin (1989), The dissolution of calcite in acid waters-mass-transport versus surface control, *Freshwater Biol.*, *22*(2), 285–288.

Cunningham, A. B., R. Gerlach, L. Spangler, and A. C. Mitchell (2009), Microbially enhanced geologic containment of sequestered supercritical CO_2, *Energy Procedia*, *1*(1), 3245–3252.

Cunningham, A. B., R. Gerlach, L. Spangler, A. C. Mitchell, S. Parks, and A. Phillips (2011), Reducing the risk of well bore leakage of CO_2 using engineered biomineralization barriers, *Energy Procedia*, *4*, 5178–5185.

Cuthbert, M. O., M. S. Riley, S. Handley-Sidhu, J. C. Renshaw, D. J. Tobler, V. R. Phoenix, and R. Mackay (2012), Controls on the rate of ureolysis and the morphology of carbonate precipitated by *S. Pasteurii* biofilms and limits due to bacterial encapsulation, *Ecol. Eng.*, *41*(0), 32–40.

DeJong, J. T. (2006), Microbially induced cementation to control sand response to undrained shear, *J. Geotech. Geoenviron. Eng.*, *132*(11), 1381.

DeJong, J. T., B. M. Mortensen, B. C. Martinez, and D. C. Nelson (2010), Bio-mediated soil improvement, *Ecol. Eng.*, *36*(2), 197–210.

DeJong, J. T., K. Soga, S. A. Banwart, W. R. Whalley, T. R. Ginn, D. C. Nelson, B. M. Mortensen, B. C. Martinez, and T. Barkouki (2012), Soil engineering in vivo: Harnessing natural biogeochemical systems for sustainable, multi-functional engineering solutions, *J. R. Soc., Interface*, *8*(54), 1–15.

De Muynck, W., N. De Belie, and W. Verstraete (2010a), Microbial carbonate precipitation in construction materials: A review, *Ecol. Eng.*, *36*(2), 118–136.

De Muynck, W., K. Verbeken, N. De Belie, and W. Verstraete (2010b), Influence of urea and calcium dosage on the effectiveness of bacterially induced carbonate precipitation on limestone, *Ecol. Eng.*, *36*(2), 99–111.

Duan, Z., and R. Sun (2003), An improved model calculating CO_2 solubility in pure water and aqueous NaCl solutions from 273 to 533 K and from 0 to 2000 bar, *Chem. Geol.*, *193*, 257–271.

Dupraz, S., B. Menez, P. Gouze, R. Leprovost, P. Benezeth, O. S. Pokrovsky, and F. Guyot (2009a), Experimental approach of CO_2 biomineralization in deep saline aquifers, *Chem. Geol.*, *265*(1–2), 54–62.

Dupraz, S., M. Parmentier, B. Menez, and F. Guyot (2009b), Experimental and numerical modeling of bacterially induced pH increase and calcite precipitation in saline aquifers, *Chem. Geol.*, *265*(1–2), 44–53.

Ebigbo, A., R. Helmig, A. B. Cunningham, H. Class, and R. Gerlach (2010), Modelling biofilm growth in the presence of carbon dioxide and water flow in the subsurface, *Adv. Water Resour.*, *33*(7), 762–781.

Fauriel, S., and L. Laloui (2011), A bio-hydro-mechanical model for propagation of biogrout in soils, in *Geo-Frontiers 2011 Conference, ASCE, Dallas, Texas*, edited by J. Han and D. A. Alzamora, pp. 4041–4048, Am. Soc. of Civil Engin., Reston, Virginia.

Fenghour, A., W. A. Wakeham, and V. Vesovic (1998), The viscosity of carbon dioxide, *J. Phys. Chem. Ref. Data*, *27*(1), 31–44.

Ferris, F., L. Stehmeier, A. Kantzas, and F. Mourits (1996), Bacteriogenic mineral plugging, *J. Can. Petrol. Technol.*, *35*, 56–61.

Ferris, F., V. Phoenix, Y. Fujita, and R. Smith (2003), Kinetics of calcite precipitation induced by ureolytic bacteria at 10 to 20 degrees C in artificial groundwater, *Geochim. Cosmochim. Acta*, *67*(8), 1701–1710.

Fidaleo, M., and R. Lavecchia (2003), Kinetic study of enzymatic urea hydrolysis in the pH range 4–9, *Chem. Biochem. Eng. Q.*, *17*(4), 311–318.

Flukiger, F., and D. Bernard (2009), A new numerical model for pore scale dissolution of calcite due to CO_2 saturated water flow in 3D realistic geometry: Principles and first results, *Chem. Geol.*, *265*(1–2), 171–180.

Frippiat, C. C., P. C. Prez, and A. E. Holeyman (2008), Estimation of laboratory-scale dispersivities using an annulus-and-core device, *J. Hydrol.*, *362*(1–2), 57–68.

Fujita, Y., G. D. Redden, J. C. Ingram, M. M. Cortez, F. G. Ferris, and R. W. Smith (2004), Strontium incorporation into calcite generated by bacterial ureolysis, *Geochim. Cosmochim. Acta*, *68*(15), 3261.

Fujita, Y., J. L. Taylor, T. L. T. Gresham, M. E. Delwiche, F. S. Colwell, T. L. McLing, L. M. Petzke, and R. W. Smith (2008), Stimulation of microbial urea hydrolysis in groundwater to enhance calcite precipitation, *Environ. Sci. Technol.*, *42*(8), 3025–3032.

Fujita, Y., J. Taylor, L. Wendt, D. Reed, and R. Smith (2010), Evaluating the potential of native ureolytic microbes to remediate a (90)sr contaminated environment, *Environ. Sci. Technol.*, *44*(19), 7652–7658.

Golfier, F., B. D. Wood, L. Orgogozo, M. Quintard, and M. Buès (2009), Biofilms in porous media: Development of macroscopic transport equations via volume averaging with closure for local mass equilibrium conditions, *Adv. Water Resour.*, *32*, 463–485.

Hao, O. J., M. G. Richard, D. Jenkins, and H. W. Blanch (1983), The half-saturation coefficient for dissolved-oxygen—a dynamic method for its determination and its effect on dual species competition, *Biotechnol. Bioeng.*, *25*(2), 403–416.

Harkes, M. P., L. A. van Paassen, J. L. Booster, V. S. Whiffin, and M. C. M. van Loosdrecht (2010), Fixation and distribution of bacterial activity in sand to induce carbonate precipitation for ground reinforcement, *Ecol. Eng.*, *36*(2), 112–117.

Helmig, R., H. Class, R. Huber, H. Sheta, R. Ewing, R. Hinkelmann, H. Jakobs, and P. Bastian (1998), Architecture of the modular program system MUFTE-UG for simulating multiphase flow and transport processes in heterogeneous porous media, *Math. Geol.*, *2*, 123–131.

Ivanov, V., and J. Chu (2008), Applications of microorganisms to geotechnical engineering for bioclogging and biocementation of soil in situ, *Rev. Environ. Sci. Biotechnol.*, *7*(2), 139–153.

Ji, J. (1994), Fundamental aspects of nickel electrowinning from chloride electrolytes, Ph.D. thesis, University of British Columbia, Canada, 267 pp.

Kim, D.-S., and H. S. Fogler (2000), Biomass evolution in porous media and its effects on permeability under starvation conditions, *Biotechnol. Bioeng.*, *69*(1), 47–56.

Kim, D. S., S. Thomas, and H. S. Fogler (2000), Effects of pH and trace minerals on long-term starvation of *Leuconostoc mesenteroides*, *Appl. Environ. Microbiol.*, *66*(3), 976–981.

Klose, S., and M. A. Tabatabai (1999), Urease activity of microbial biomass in soils, *Soil Biol. Biochem.*, *31*(2), 205–211.

Krajewska, B. (2009), Ureases I. Functional, catalytic and kinetic properties: A review, *J. Mol. Catal. B: Enzym.*, *59*(1–3), 9–21.

Li, Y.-H., Y.-Y. M. Chen, and R. A. Burne (2000), Regulation of urease gene expression by *Streptococcus salivarius* growing in biofilms, *Environ. Microbiol.*, *2*(2), 169–177.

Lloyd, A. B., and M. J. Sheaffe (1973), Urease activity in soils, *Plant Soil*, *39*, 71–80.

Mateles, R. I. (1971), Calculation of the oxygen required for cell production, *Biotechnol. Bioeng.*, *13*(4), 581–582.

Melo, L. F. (2005), Biofilm physical structure, internal diffusivity and tortuosity, *Water Sci. Technol.*, *52*(7), 77–84.

Michaelides, E. E. (1981), Thermodynamic properties of geothermal fluids, *Trans. – Geotherm. Resour. Counc.*, *5*, 361–364.

Millero, F., F. Huang, T. Graham, and D. Pierrot (2007), The dissociation of carbonic acid in NaCl solutions as a function of concentration and temperature, *Geochim. Chosmochim. Acta. 71*(1), 46–55.

Millero, F. J., P. J. Milne, and V. L. Thurmond (1984), The solubility of calcite, strontianite and witherite in NaCl solutions at 25°C, *Geochim. Chosmochim. Acta.*, *48*(5), 1141–1143.

Millington, R., and J. P. Quirk (1961), Permeability of porous solids, *Trans. Faraday Soc.*, *57*(8), 1200–1207.

Mitchell, A. C., and F. G. Ferris (2006), The influence of *Bacillus pasteurii* on the nucleation and growth of calcium carbonate, *Geomicrobiol. J.*, *23*(3–4), 213–226.

Mitchell, A. C., A. J. Phillips, M. A. Hamilton, R. Gerlach, W. K. Hollis, J. P. Kaszuba, and A. B. Cunningham (2008), Resilience of planktonic and biofilm cultures to supercritical CO_2, *J. Supercritical Fluids*, *47*(2), 318–325.

Mobley, H. L. T., and R. P. Hausinger (1989), Microbial ureases-significance, regulation, and molecular characterization, *Microbiol. Rev.*, *53*(1), 85–108.

Mortensen, B., M. Haber, J. DeJong, L. Caslake, and D. Nelson (2011), Effects of environmental factors on microbial induced calcium carbonate precipitation, *J. Appl. Microbiol.*, *111*(2), 338–349.

Murphy, E. M., and T. R. Ginn (2000), Modeling microbial processes in porous media, *Hydrogeol. J.*, *8*(1), 142–158.

Norland, S., M. Heldal, and O. Tumyr (1987), On the relation between dry-matter and volume of bacteria, *Microbial Ecol.*, *13*(2), 95–101.

Parks, S. L. (2009), Kinetics of calcite precipitation by ureolytic bacteria under aerobic and anaerobic conditions, Master's thesis, Montana State University, Bozeman.

Resch, A., R. Rosenstein, C. Nerz, and F. Gotz (2005), Differential gene expression profiling of *Staphylococcus aureus* cultivated under biofilm and planktonic conditions, *Appl. Environ. Microbiol.*, *71*(5), 2663–2676.

Rittmann, B. E. (1982), The effect of shear stress on biofilm loss rate, *Biotechnol. Bioeng.*, *24*(2), 501–506.

Rockhold, M. L., R. R. Yarwood, and J. S. Selker (2004), Coupled microbial and transport processes in soils, *Vadose Zone J.*, *3*(2), 368–383.

Schultz, L., B. Pitts, A. C. Mitchell, A. B. Cunningham, and R. Gerlach (2011), Imaging biologically induced mineralization in fully hydrated flow systems, *Microscopy Today*, *19*(05), 12–15.

Seto, M., and M. Alexander (1985), Effect of bacterial density and substrate concentration on yield coefficients, *Appl. Environ. Microbiol.*, *50*(5), 1132–1136.

Span, R., and W. Wagner (1996), A new equation of state for carbon dioxide covering the fluid region from the triple-point temperature to 1100 K at pressures up to 800 MPa, *J. Phys. Chem. Ref. Data*, *25*(6), 1509–1596.

Speitel, G. E., and F. A. DiGiano (1987), Biofilm shearing under dynamic conditions, *J. Environ. Eng.*, *113*(3), 464–475.

Stumm, W., and J. J. Morgan (1996), *Aquatic Chemistry: Chemical Equilibria and Rates in Natural Waters*, 3rd ed., xvi, 1022 pp., Wiley, N. Y.

Tanyolac, A., and H. Beyenal (1997), Prediction of average biofilm density and performance of a spherical bioparticle under substrate inhibition, *Biotechnol. Bioeng.*, *56*(3), 319–329.

Taylor, S. W., and P. R. Jaffé (1990), Substrate and biomass transport in a porous medium, *Water Resour. Res.*, *26*(9), 2181–2194.

Tobler, D. J., M. O. Cuthbert, R. B. Greswell, M. S. Riley, J. C. Renshaw, S. Handley-Sidhu, and V. R. Phoenix (2011), Comparison of rates of ureolysis between *Sporosarcina pasteurii* and an indigenous groundwater community under conditions required to precipitate large volumes of calcite, *Geochim. Cosmochim. Acta*, *75*(11), 3290–3301, doi:10.1016/j.gca.2011.03.023.

van Duijn, C. J., and I. S. Pop (2004), Crystal dissolution and precipitation in porous media: Pore scale analysis, *J. Für Die Reine Und Angewandte Mathematik*, *577*, 171–211.

van Noorden, T. L. (2009a), Crystal precipitation and dissolution in a porous medium: Effective equations and numerical experiments, *Multiscale Mode. Simul.*, *7*(3), 1220–1236.

van Noorden, T. L. (2009b), Crystal precipitation and dissolution in a thin strip, *Eur. J. Appl. Math.*, *20*, 69–91.

van Noorden, T. L., I. S. Pop, A. Ebigbo, and R. Helmig (2010), An upscaled model for biofilm growth in a thin strip, *Water Resour. Res.*, *46*, W06505, doi:10.1029/2009WR008217.

van Paassen, L. A., R. Ghose, T. J. M. van der Linden, W. R. L. van der Star, and M. C. M. van Loosdrecht (2010), Quantifying biomediated ground improvement by ureolysis: Large-scale biogrout experiment, *J. Geotech. Geoenviron. Eng.*, *136*(12), 1721–1728.

van Wijngaarden, W., F. Vermolen, G. Meurs, and C. Vuik (2011), Modelling biogrout: A new ground improvement method based on microbial-induced carbonate precipitation, *Transp. Porous Media*, *87*(2), 397–420.

Whiffin, V. S., L. A. van Paassen, and M. P. Harkes (2007), Microbial carbonate precipitation as a soil improvement technique, *Geomicrobiol. J.*, *24*(5), 417–423.

Wolf, M., O. Breitkopf, and R. Puk (1989), Solubility of calcite in different electrolytes at temperatures between 10° and 60°C and at CO_2 partial pressures of about 1 kPa, *Chem. Geol.*, *76*(3–4), 291–301.

Xu, T. F., Y. Ontoy, P. Molling, N. Spycher, M. Parini, and K. Pruess (2004), Reactive transport modeling of injection well scaling and acidizing at Tiwi field, Philippines, *Geothermics*, *33*(4), 477–491.

Zhang, T., and I. Klapper (2010), Mathematical model of biofilm induced calcite precipitation, *Water Sci. Technol.*, *61*(11), 2957–2964.

Zhang, T. C., and P. L. Bishop (1994), Density, porosity, and pore structure of biofilms, *Water Res.*, *28*(11), 2267–2277.

Zhong, S. J., and A. Mucci (1989), Calcite and aragonite precipitation from seawater solutions of various salinites—precipitation rates and overgrowth compositions, *Chem. Geol.*, *78*(3–4), 283–299.